

# 4D Visualization of a Nonthermal Coherent Magnon in a Laser Heated Lattice by an X-ray Free Electron Laser

Hoyoung Jang, Hiroki Ueda, Hyeong-Do Kim, Minseok Kim, Kwang Woo Shin, Kee Hoon Kim, Sang-Youn Park, Hee Jun Shin, Pavel Borisov, Matthew J. Rosseinsky, Dogeun Jang, Hyeonggi Choi, Intae Eom, Urs Staub, and Sae Hwan Chun\*

Ultrafast optical manipulation of magnetic phenomena is an exciting achievement of mankind, expanding one's horizon of knowledge toward the functional nonequilibrium states. The dynamics acting on an extremely short timescale push the detection limits that reveal fascinating light–matter interactions for nonthermal creation of effective magnetic fields. While some cases are benchmarked by emergent transient behaviors, otherwise identifying the nonthermal effects remains challenging. Here, a femtosecond time-resolved resonant magnetic X-ray diffraction experiment is introduced, which uses an X-ray free-electron laser (XFEL) to distinguish between the effective field and the photoinduced thermal effect. It is observed that a multiferroic Y-type hexaferrite exhibits magnetic Bragg peak intensity oscillations manifesting entangled antiferromagnetic (AFM) and ferromagnetic (FM) Fourier components of a coherent AFM magnon. The magnon trajectory constructed in 3D space and time domains is decisive to evince ultrafast field formation preceding the lattice thermalization. A remarkable impact of photoexcitation across the electronic bandgap is directly unraveled, amplifying the photomagnetic coupling that is one of the highest among AFM dielectrics. Leveraging the above-bandgap photoexcitation, this energy-efficient optical process further suggests a novel photomagnetic control of ferroelectricity in multiferroics.

## 1. Introduction

Magnetism maneuverable by an ultrashort optical laser pulse represents an outstanding showcase that illuminates intriguing light interactions with fundamental physical degrees of freedom in condensed matter.<sup>[1–3]</sup> Apart from the magnetic field component of the electromagnetic wave, the light–matter interactions may produce an internal effective magnetic field through relativistic spin–orbital coupling (spin/orbital degrees of freedom),<sup>[4–6]</sup> resonant electronic transitions (charge degree of freedom),<sup>[7–8]</sup> and direct optical pumping of phonons (lattice degree of freedom).<sup>[9–12]</sup> Each of the processes commences nonthermally by the photoirradiation, being dissociated with the photoinduced thermal effect.<sup>[13]</sup> The fascinating physics uncovered in these processes have contributed to the current research paradigm of investigating photoinduced nonequilibrium states in quantum materials.<sup>[14]</sup> The emerging research field of optospintronics regards those nonthermal effects as innovative

H. Jang, H.-D. Kim, M. Kim, S.-Y. Park, H. J. Shin, D. Jang, H. Choi,  
I. Eom, S. H. Chun  
Pohang Accelerator Laboratory  
POSTECH  
Pohang, Gyeongbuk 37673, Republic of Korea  
E-mail: saehwan.chun@postech.ac.kr  
H. Jang, I. Eom, S. H. Chun  
Photon Science Center  
POSTECH  
Pohang, Gyeongbuk 37673, Republic of Korea

H. Ueda, U. Staub  
Swiss Light Source  
Paul Scherrer Institute  
Villigen-PSI 5232, Switzerland  
H. Ueda  
SwissFEL  
Paul Scherrer Institute  
Villigen-PSI 5232, Switzerland  
K. W. Shin, K. H. Kim  
Center for Novel States of Complex Materials Research  
Department of Physics and Astronomy  
Seoul National University  
Seoul 08826, Republic of Korea  
P. Borisov  
Department of Physics  
Loughborough University  
Loughborough LE11 3TU, UK  
P. Borisov, M. J. Rosseinsky  
Department of Chemistry  
University of Liverpool  
Liverpool L7 3NY, UK

 The ORCID identification number(s) for the author(s) of this article can be found under <https://doi.org/10.1002/adma.202303032>

© 2023 The Authors. Advanced Materials published by Wiley-VCH GmbH. This is an open access article under the terms of the Creative Commons Attribution License, which permits use, distribution and reproduction in any medium, provided the original work is properly cited.

DOI: 10.1002/adma.202303032

pathways to accomplish ultrafast control of the magnetic moment.<sup>[1–3]</sup>

A variety of nonthermal ways to create an effective field have been identified with the aid of time-resolved optical spectroscopy experiments.<sup>[4–12,15–23]</sup> However, the fact that the optical techniques also sense photoinduced changes in other degrees of freedom makes it nontrivial to distinguish the nonthermally created field from the photoinduced thermal effect. While some cases can be attested by transient magnetic behaviors distinct from the static ones at the elevated temperature, e.g., pump-light polarization dependences,<sup>[4,5,16–18]</sup> or emergent new properties,<sup>[11,24]</sup> or inferred by using a low pump fluence supposed to increase temperature insignificantly,<sup>[25,26]</sup> if neither of these criteria is applicable, it becomes challenging to identify the origin of magnetic dynamics. For dielectric materials, photoexcitation above the electronic bandgap is one of the most effective ways to optically manipulate material properties based on large amount of the photoexcited charge carriers coupled to the other physical degrees of freedom.<sup>[14,27–29]</sup> However, for the study of the nonthermal field effects, this approach has been largely avoided because of the great confusion with thermal effect caused by formidable light absorption. If one has experimental probes that are able to differentiate the dynamics of spin and the other degrees of freedom, the gateway to revealing nonthermal magnetic effects can be widely open.

The recent development of X-ray free electron lasers (XFELs) has made a breakthrough to extend various X-ray spectroscopy and scattering techniques into ultrafast time domain based on femtosecond X-ray pulses with high brightness.<sup>[30]</sup> In this work, we devise time-resolved resonant magnetic X-ray diffraction to discriminate a nonthermally created magnetic field against the photoinduced thermal effect in a multiferroic Y-type hexaferrite. A coherent magnon trajectory visualized in 4D domains, i.e., 3D space and 1D time, manifests sub-picosecond formation of the effective field followed by delayed lattice thermalization of  $\approx 10$  ps. The 4D trajectory allows us to directly quantify the field strength for both below- and above-bandgap photoexcitations, and in turn unveils a large amplification of the photoinduced field for the latter. This observation underscores a highly energy-efficient route to achieve substantial field strength desired for optospintronics applications.<sup>[31,32]</sup> The scope of the applications even broadens for multiferroics with magnetic and electric dipoles strongly coupled to each other, in the perspective of that the optically manipulated magnetic moment is functional for controlling the ferroelectric polarization.<sup>[33–35]</sup>

## 2. Results and Discussion

### 2.1. Photoinduced Intensity Oscillations in Magnetic Bragg Reflections

The Y-type hexaferrite studied in this work is  $\text{Ba}_{0.5}\text{Sr}_{1.5}\text{Zn}_2(\text{Fe}_{1-x}\text{Al}_x)_{12}\text{O}_{22}$  ( $x = 0.08$ , BSZFAO), a multiferroic material that features magnetically-induced ferroelectric polarization ( $P_{\text{FE}}$ ).<sup>[36]</sup> It has a transverse conical magnetic order, i.e., a canted AFM structure with a cycloid spin component, which involves inverse Dzyaloshinskii–Moriya interaction in creating  $P_{\text{FE}}$  (Figure 1a).<sup>[36,37]</sup> The notion that this magnetic order persists close to or even at room temperature (for

$x = 0.00$ ) has drawn significant attention as a rare example of room-temperature magnetoelectrics.<sup>[38]</sup> We choose the  $x = 0.08$  compound marking a giant magnetoelectric coupling that enables  $P_{\text{FE}}$  to be switched by a small magnetic field of  $<10$  mT.<sup>[36]</sup> We anticipate that the photoinduced effective magnetic field in this multiferroic not only controls the magnetization but also potentially manipulates  $P_{\text{FE}}$ .

Its transverse conical magnetic order consists of FM and AFM components from the net magnetic moments  $\mu_L$  and  $\mu_S$  of the structural  $L$  (large) and  $S$  (small) blocks, respectively (Figure 1a).<sup>[37]</sup> For instance, the external magnetic field along the  $x$ -axis in the  $ab$ -plane aligns the FM component of  $\mu_L$  ( $\mathbf{m} = \mu_{L1+} + \mu_{L2}$ ) along the field and the AFM component of  $\mu_L$  ( $\mathbf{l} = \mu_{L1} - \mu_{L2}$ ) along the orthogonal  $y$ -axis in the  $ab$ -plane. Meanwhile,  $\mu_S$  directs its FM component opposite to the field and AFM component along the  $z$ -axis perpendicular to the  $ab$ -plane. These individual sublattices of  $\mu_L$  and  $\mu_S$  give rise to FM ( $0\ 0\ 3n$ ) and AFM ( $0\ 0\ 3n \pm 1.5$ ) Bragg reflections with integer  $n$ . These reflections can be probed using resonant soft X-ray diffraction near the Fe  $L_3$  edge ( $\approx 710$  eV), owing to the long  $c$ -axis parameter of BSZFAO ( $c = 43.3$  Å,  $a = b = 5.85$  Å) (Figure 1b,c). Figure 1d summarizes the experimental layout, where an external magnetic field is applied normal to the horizontal scattering plane. This geometry allows the  $\pi$ – $\pi'$  and  $\pi$ – $\sigma'$  polarization channels to selectively detect the FM and AFM components, projecting each component on the  $x$ -axis and the incident X-ray direction ( $\parallel \mathbf{k}_i$ ), respectively.

We employ the optical laser pump and X-ray probe experiment to investigate temporal changes of the magnetic Bragg reflections. The transverse conical magnetic structure is stable below 260 K with an external magnetic field ( $H_{\text{ext}}$ ) applied along the  $ab$ -plane. To prepare the magnetic state, the sample was cooled from 300 K (above the magnetic transition temperature) down to 82 K (the base temperature of the liquid-nitrogen cryostat) with  $H_{\text{ext}} = 200$  mT ( $\parallel ab$ -plane) applied during the cooling process (Figure 1d). The pump–probe experiment was conducted mostly at the base temperature because the oscillating features in the magnetic Bragg peak intensities could be clearly shown. The optical laser with the wavelength ( $\lambda_{\text{laser}}$ ) = 400 nm was used to excite the valence electrons above the direct bandgap (Figure S1, Supporting Information).<sup>[39]</sup> We tuned the X-ray to the incident energy ( $E_i$ ) = 702 eV, with an energy of a few eV below the Fe  $L_3$  edge, which penetrates deep into the material and probes the bulk properties (see Experimental Section). Figure 2a shows the transient intensities of FM ( $0\ 0\ 3$ ), AFM ( $0\ 0\ 1.5$ ), and ( $0\ 0\ 4.5$ ) Bragg reflections as a function of time delay after the photoirradiation. We observe that these Bragg peaks display multiple oscillation cycles with a period of  $24 \pm 0.5$  ps. Their Fourier transformation shows a single oscillation frequency centered at  $41.7 \pm 0.9$  GHz ( $\approx 0.17$  meV), implying a quasiparticle state present with the corresponding energy (see Figure S3, Supporting Information).

Quasiparticles such as coherent phonons or magnons are able to oscillate Bragg reflection intensities. We first inspect the relevance of coherent phonon for the oscillating feature. The resonant FM ( $0\ 0\ 3$ ) Bragg peak contains structure factors not only from the FM component but also from the crystal structure and the orbital asphericity. If the coherent phonon is the origin of intensity oscillation in the middle panel of Figure 2a, the same oscillation will be present in a non-resonant condition suppressing

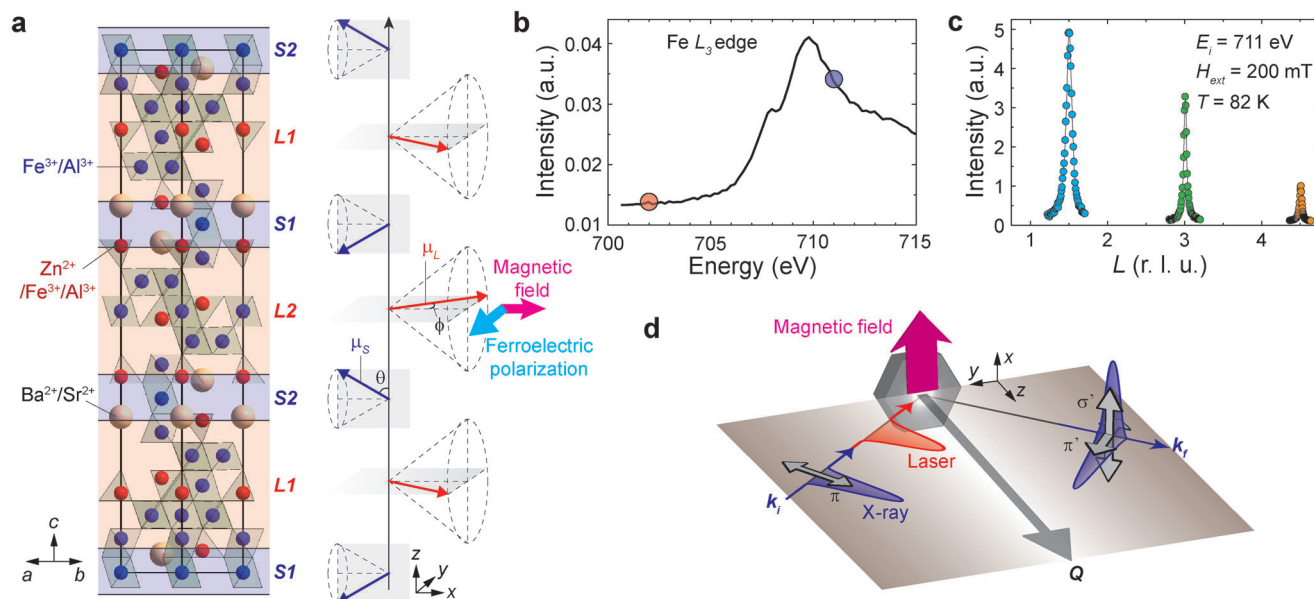


**Figure 1.** Crystal and magnetic structures of the Y-type hexaferrite and experimental layout for the time-resolved resonant magnetic X-ray diffraction. a) The crystallographic unit cell (left) consists of multiple Fe/Al (blue)-O octahedra and Zn/Fe/Al (red)-O tetrahedra that construct magnetic L<sub>1,2</sub> (orange rectangles) and S<sub>1,2</sub> blocks (blue rectangles). The oxygen anions at the vertices are not shown for simplicity. The canted AFM magnetic structure (right) is represented by net magnetic moments of the L (μ<sub>L</sub>, red arrow) and S (μ<sub>S</sub>, blue arrow) blocks under the external magnetic field, H<sub>ext</sub> || +x. The μ<sub>L</sub> and μ<sub>S</sub> are constrained in horizontal and vertical planes (gray), respectively. The μ<sub>L</sub> and μ<sub>S</sub> lead to the cycloidal spin components in the yz-plane with the modulation || the z-axis, yielding the ferroelectric polarization || the y-axis. The dotted black frames are guides to the eye for conceiving the transverse conical structure. The φ and θ are angles between the μ<sub>L</sub> and the x-axis, and between the μ<sub>S</sub> and the z-axis, respectively. b) X-ray absorption spectrum at the Fe L<sub>3</sub> edge. The circles denote the incident X-ray energies used in this work. c) L-scan covering FM (0 0 3), AFM (0 0 1.5), and (0 0 4.5) Bragg peaks at T = 82 K using an incident X-ray photon energy, E<sub>i</sub> = 711 eV. d) Layout of the time-resolved resonant magnetic X-ray diffraction. The horizontal scattering plane (gray gradient) is defined by the incident (k<sub>i</sub>) and outgoing (k<sub>f</sub>) wavevectors. Optical laser (red) and X-ray (blue) pulses are collinearly incident on the sample with the polarizations lying in the scattering plane, i.e., p- and π-polarizations, respectively, while the diffracted X-ray pulse has both π'- and σ'-polarizations.

the magnetic contribution. It turns out such an oscillation is not shown in the non-resonant (0 0 3) reflection (shown later in Figure 4). Thus, we turn our attention to the coherent magnon as the possible origin. We observe that reversing an external magnetic field inverts the oscillation profiles of the AFM (0 0 4.5) Bragg reflection, while the profiles of the FM (0 0 3) Bragg reflection remain unaffected (Figure 2b,c). Notably, an AFM magnon with μ<sub>L1</sub> and μ<sub>L2</sub> precessing counter-clockwise around quasi-equilibrium positions fully explains the oscillation profiles of the AFM (0 0 4.5) and FM (0 0 3) intensities (Figure 2d). For example, the AFM precession projected on the scattering plane for H<sub>ext</sub> || +x (Figure 2e) realizes that the AFM (0 0 4.5) intensity (∝|l · k<sub>f</sub>|<sup>2</sup>) minimizes at π/2-phase (every first quarter period) and maximizes at 3π/2-phase (every third quarter period). Meanwhile, the FM (0 0 3) intensity (∝|m · x|<sup>2</sup>) minimizes at π-phase (every half period) and maximizes at 2π-phase (every full period). These relations result in inverted-sinusoidal and cosinusoidal profiles in the AFM (0 0 4.5) and FM (0 0 3) Bragg reflections, respectively. On the other hand, when H<sub>ext</sub> is reversed || -x, the μ<sub>L</sub> and its precession trajectory are rotated by 180° around the z-axis (Figure 2f): the AFM component precessing on the scattering plane is reversed, while the FM component out of the plane keeps the mirrorsymmetry. As the consequence, the AFM and FM profiles are inverted and maintained, i.e., sinusoidal and cosinusoidal, respectively (Figure 2b,c). We confirm that the other combinations of the precessing motions are incompatible with the

intensity oscillations in Figure 2a–c (see Note S4 and Figures S5–S8, Supporting Information).

## 2.2. An Effective Magnetic Hamiltonian Quantifying the Precessing Magnetic Moment

An effective magnetic Hamiltonian model provides a further understanding of the coherent AFM magnon. This Hamiltonian is built from the L and S blocks:<sup>[40,41]</sup>

$$\begin{aligned} \mathcal{H} = & J_{LS} \sum_{i,j=1,2} \vec{\mu}_{Si} \cdot \vec{\mu}_{Lj} + 2J_{LL} \vec{\mu}_{L1} \cdot \vec{\mu}_{L2} + 2J_{SS} \vec{\mu}_{S1} \cdot \vec{\mu}_{S2} \\ & + D_L \sum_{i,j=1,2} (\mu_{Li}^z)^2 + D_S \sum_{i,j=1,2} (\mu_{Si}^z)^2 - H_x \sum_{i,j=1,2} (\mu_{Li}^x + \mu_{Si}^x) \end{aligned} \quad (1)$$

with J<sub>LS</sub>, J<sub>LL</sub>, and J<sub>SS</sub> being the exchange interaction constants of L and S, L and L, and S and S blocks, respectively; D<sub>L</sub> and D<sub>S</sub> are the magnetic anisotropy constants of L and S blocks along the z-axis (|| [001]), respectively, and H<sub>x</sub> is the sum of internal (H<sub>int</sub>) and external (H<sub>ext</sub>) magnetic fields along the x-axis. Most of the parameters in the Hamiltonian are determined by matching the simulation and the experimental data of the static magnetization (M<sub>x</sub>) vs magnetic field (see Experimental Section). The H<sub>ext</sub> regions

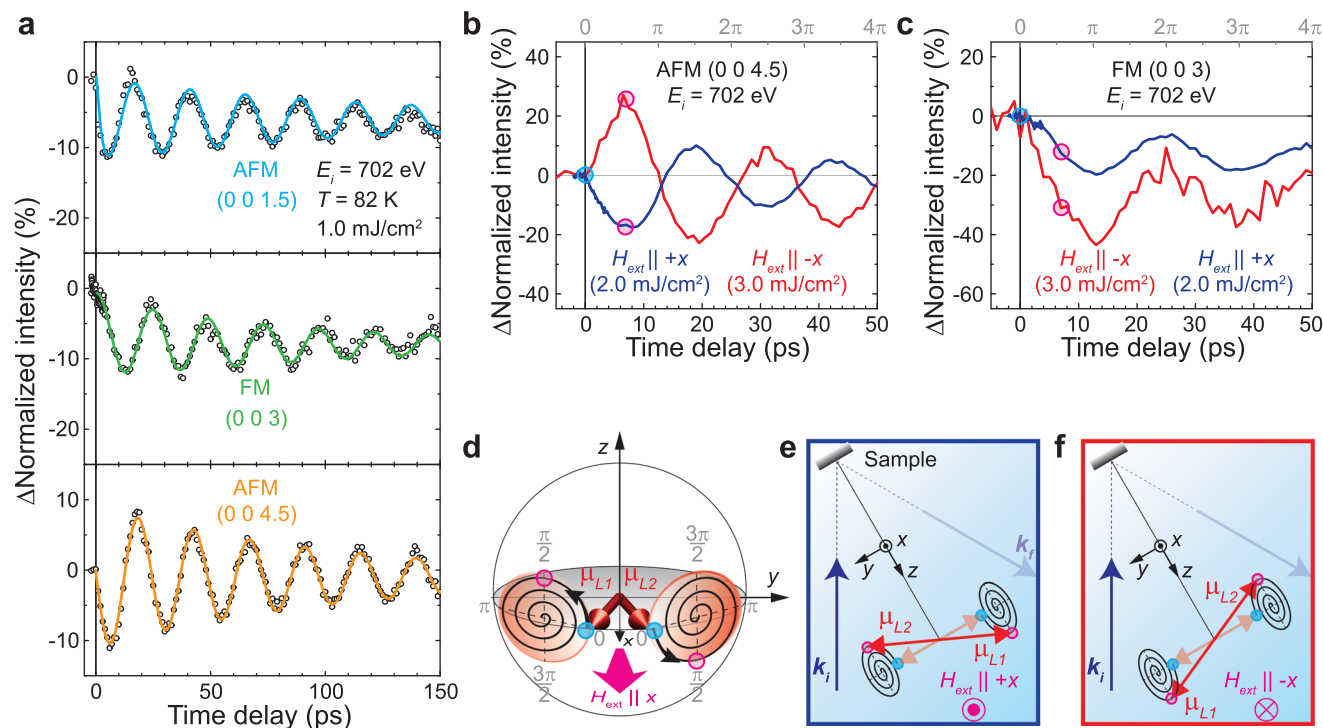


**Figure 2.** Transient magnetic Bragg peak intensities. a) AFM (0 0 1.5) (top), FM (0 0 3) (middle), and AFM (0 0 4.5) (bottom) reflections at  $T = 82$  K for a laser fluence  $= 1.0 \text{ mJ cm}^{-2}$  using  $E_i = 702$  eV. The transient data (symbols) are normalized to the intensity at a negative time delay of  $-1$  ps for each reflection. The solid lines are fitting results combining a damped oscillation and an exponential decay (Table S1, Supporting Information). b) AFM (0 0 4.5) and c) FM (0 0 3) reflections for  $H_{\text{ext}} \parallel +x$  (blue,  $2.0 \text{ mJ cm}^{-2}$ ) and  $-x$  (red,  $3.0 \text{ mJ cm}^{-2}$ ) at  $T = 82$  K. The colored circles correspond to the same colored  $\mu_L$  directions on the precession trajectory shown in (d). d) Schematic illustration of  $\mu_{L1}$  and  $\mu_{L2}$ , which precess counter-clockwise (denoted by black arrows) around the precession axes tilted further away from the  $x$ -axis. The spiral lines represent the precession trajectories toward the new equilibrium directions. e, f) Top view of the experimental geometries for  $H_{\text{ext}} \parallel +x$  (e) and  $-x$  (f). The  $\mu_L$  and its precession trajectory are projected on the horizontal scattering plane. The  $\mu_L$  at the beginning of the precession and at the first quarter of the oscillation period is denoted by the light red and dark red arrows, respectively.

displaying steep ( $<100$  mT), moderate (100 mT to 1.6 T), and gentle ( $>1.6$  T) slopes correspond to magnetic domain alignment, gradual reduction of the transverse conical angles for  $\mu_{L1}$  and  $\mu_{L2}$  down to zero, and progressive flop of  $\mu_{S1}$  and  $\mu_{S2}$  toward  $+x$  direction, respectively (Figure 3a). The  $M_x$  vs  $H_{\text{ext}}$  relation derived from the magnetic Hamiltonian is consistent with the behavior of the single magnetic domain, reproducing well the experimental data above 100 mT. Meanwhile, the magnetic anisotropy constants  $D_L$  and  $D_S$  are determined from the magnon energies calculated from the Landau–Lifshitz–Gilbert equation (see Experimental Section; Note S1, Supporting Information). Two solutions for the equation correspond to normal modes that embody distinct magnitudes of AFM precessions of  $\mu_{L1}$  and  $\mu_{L2}$ , and  $\mu_{S1}$  and  $\mu_{S2}$ . We assign the observed 41.7 GHz ( $\approx 0.17$  meV) in Figure 2 to the lower energy magnon by noting that the higher energy magnon in Y-type hexaferrites is usually located in the frequency range of 0.5–1.5 THz.<sup>[40,42,43]</sup> Using the fully determined parameters in the Hamiltonian, the relative magnitudes of  $\mu_{L1}$  and  $\mu_{S1}$  precessions are calculated (see Experimental Section; Figure S2, Supporting Information). Figure 3d illustrates the precession motion of the lower energy magnon relevant to the observed intensity oscillations. The  $\mu_L$  precession is dominant and nearly isotropic in the surface normal to the precession axis, while the  $\mu_S$  precession is insignificant and anisotropically elon-

gated along the  $x$ -axis. This calculation result verifies our data interpretation mainly with the  $\mu_L$  precession.

We note that the oscillation amplitudes measured at both magnetic reflections allow for direct quantification of the precessing magnetic moment. For a more precise quantification, we match the penetration depths between the X-ray probe and the optical laser pump by tuning the incident X-ray energy  $E_i = 711$  eV. This energy slightly above the Fe  $L_3$  absorption edge significantly decreases the X-ray penetration depth comparable to that of the optical laser pump for  $\lambda_{\text{laser}} = 400$  nm (see Experimental Section). (We avoid using the  $E_i$  right at the Fe  $L_3$  edge  $\approx 710$  eV because of the complexity of analysis caused by radically different relative spin contributions from the octahedral and tetrahedral sites at the Fe  $L_3$  edge.<sup>[44]</sup> The  $E_i = 702$  and 711 eV employed for this study capture the behaviors of the octahedral sites of which net spin contribution is parallel to the net magnetic moment.) Figure 3b shows that the AFM (0 0 4.5) intensity exhibits a large initial oscillation amplitude amounting to 28 % of the static value at the laser fluence  $= 1.0 \text{ mJ cm}^{-2}$ . This change corresponds to the situation that  $\mu_{L1}$  and  $\mu_{L2}$  move out of the  $xy$ -plane by  $4^\circ$  toward the  $+z$  and  $-z$  directions, respectively, at the first  $\pi/2$ -phase (the first quarter of the oscillation period). As the precession is nearly isotropic around the precession axis (Figure 3d), each precession axis for  $\mu_{L1}$  and  $\mu_{L2}$  tilts by the same angle toward  $-x$  direction from the



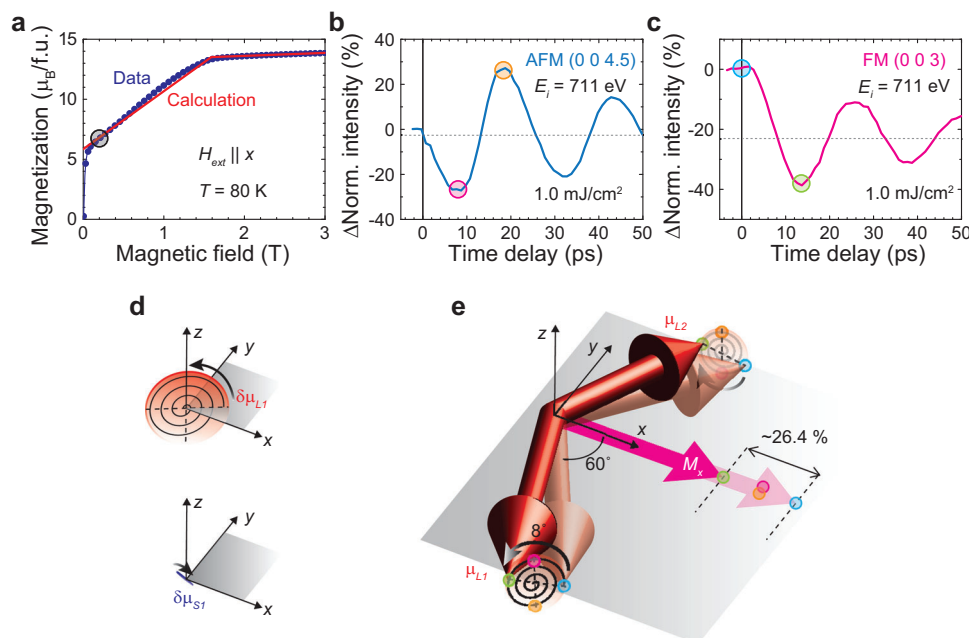


**Figure 3.** Net magnetization modified by the photoexcited AFM magnon. a)  $H_{\text{ext}}$  dependence of  $M_x$  per a formula unit (f.u.) at  $T = 80$  K presenting the experimental data (blue symbols) and calculation result (red lines) from the magnetic Hamiltonian in Equation (1). The gray circle denotes  $M_x$  at  $H_{\text{ext}}$  ( $= 200$  mT) where the X-ray diffraction experiment is performed. b) AFM (0 0 4.5) and c) FM (0 0 3) intensities at  $H_{\text{ext}} \parallel +x$  and  $T = 82$  K for a laser fluence  $= 1.0 \text{ mJ cm}^{-2}$  using incident X-ray energy,  $E_i = 711$  eV. The colored circles correspond to the same colored  $\mu_L$  directions on the precession trajectory shown in (e). d) Schematic illustration of the precession trajectories of  $\mu_{L1}$  and  $\mu_{S1}$  simulated from the magnetic Hamiltonian. e) Illustration of the magnetization (dark pink arrow along the x-axis) modified by the AFM magnon at the first half of the oscillation period.

initial position. The FM (0 0 3) intensity with the initial oscillation amplitude (Figure 3c) is consistent with that  $\mu_{L1}$  and  $\mu_{L2}$  tilt by the same angle further from the precession axis when they come back on the  $xy$ -plane at the  $\pi$ -phase (the half period). This precession is able to change the net-magnetization substantially. The  $M_x$  vs  $H_{\text{ext}}$  relation derived from the magnetic Hamiltonian (Figure 3a) deduces  $\Delta M_x = -1.8 \mu_B/\text{f.u.}$  ( $\approx 26.4\%$  of the static  $M_x$ ) at the first  $\pi$ -phase (the first half period) and  $\Delta M_x = -0.9 \mu_B/\text{f.u.}$  at longer time delays when  $\mu_{L1}$  and  $\mu_{L2}$  point along their precession axis at the transient quasi-equilibrium (Figure 3e).

### 2.3. Time Scale of the Lattice Thermalization

A study of time-resolved optical spectroscopy measurement suggested that photoinduced thermal changes in the magnetic exchange interactions and anisotropy energies may result in the quasi-equilibrium magnetic structure in the Y-type hexaferrite.<sup>[40]</sup> However, we find that the substantial magnetization change observed in Figure 3 is not relevant for the photoinduced thermal effect. If the thermal effect were dominant, the AFM (0 0 4.5) and FM (0 0 3) intensities would decrease by a comparable amount, in accordance with the temperature dependence of the magnetic Bragg peak intensities observed in neutron scattering.<sup>[37]</sup> This assessment is contradicted with the quasi-equilibrium intensities (the dotted offset lines in Figure 3b,c) that exhibit  $-3\%$  of the AFM (0 0 4.5) reflection, much less than the amount  $-23\%$  of the FM (0 0 3) reflection. In order to confirm ultrafast nonthermal formation of offsets, we examine the transient intensities by subtracting the oscillatory contributions (see

Figure S9, Supporting Information). It is noted that the offset of the FM (0 0 3) reflection intensity emerges on a resolution-limited short timescale, implying a nonthermal origin. [The initiation of small offset for the AFM (0 0 4.5) reflection is hard to resolve precisely as it is influenced by the remaining oscillatory feature that is not completely subtracted from the data.] At long timescales, there may be a thermal contribution to the transient intensities. However, our observation in Figure 3b,c (also Figure S9, Supporting Information) indicates that this thermal contribution does not significantly impact the nonthermal effect for laser fluences below  $2 \text{ mJ cm}^{-2}$ .

To confirm the irrelevance of the thermal effect to the observed substantial magnetization change, we inspect the timescale for the lattice to be heated by the photoirradiation with a higher fluence ( $8.3 \text{ mJ cm}^{-2}$ ). We note that the FM (0 0 3) Bragg peak contains the crystal structure factor and its radial profile (e.g.,  $\theta$ - $2\theta$  scan) serves as an indicator of the lattice response. Figure 4b shows the time-delay dependence of the peak shifts and widths obtained by fits to a Lorentzian for the  $\theta$ - $2\theta$  scans (Figure 4a). It is evident that the Bragg peak shifts to a lower angle after 10 ps manifesting a lattice expansion while the rapid increase of the peak width around the same time delay indicates sizable strain gradient during the lattice expansion. The lattice response is also checked by the non-resonant X-ray diffraction at  $E_i = 652$  eV tuned away from the X-ray absorption edges of any atomic element in the BSZFAO (Figure 4c). It appears no pronounced oscillation in the transient (0 0 3) Bragg peak intensity, but substantial intensity decrease after 10 ps followed by a saturation after 50 ps. This intensity change shows a monotonic dependence with the fluence, indicative of photoinduced thermal effects with

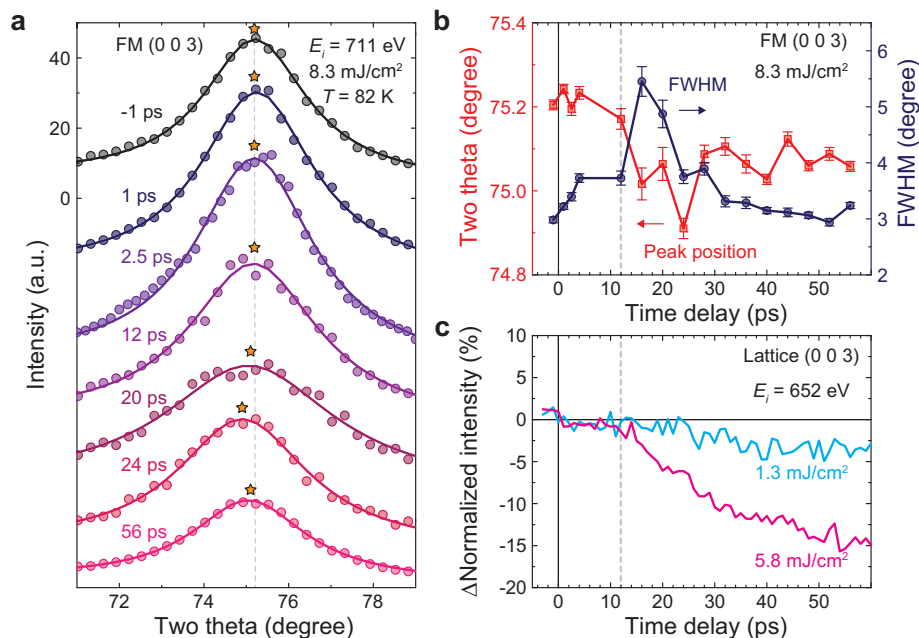


**Figure 4.** Transient response of the lattice to the laser excitation. a) The  $\theta$ - $2\theta$  scans of the (0 0 3) peak at selected time delays for a high laser fluence  $= 8.3 \text{ mJ cm}^{-2}$  of the photoirradiation with  $\lambda_{\text{laser}} = 400 \text{ nm}$  (above the bandgap). The data (circles) obtained at  $T = 82 \text{ K}$  under the resonant condition  $E_i = 711 \text{ eV}$  are fitted with a Lorentzian profile (solid line) and vertically shifted for clarity. Each fitted peak position is indicated by a star symbol and the position at  $-1 \text{ ps}$  is denoted with a vertical dashed line. b) Summary of the fitted peak position (red square, left axis) and peak width (blue circle, right axis) in the FWHM as a function of time delay. The error bars are the standard deviation of the fit. c) Normalized intensity changes at  $T = 82 \text{ K}$  under a non-resonant condition  $E_i = 652 \text{ eV}$  for laser fluences of  $1.3 \text{ mJ cm}^{-2}$  (cyan) and  $5.8 \text{ mJ cm}^{-2}$  (pink). This intensity change shows a monotonic dependence on the fluence, indicative of photoinduced thermal effects, a combination of the Debye–Waller factor, the peak shift (expansion) and width change (correlation length). The vertical dashed line (gray) depicts the onset of the peak shift and intensity change noticed in (b) and (c).

a combination of the Debye–Waller factor and the peak shift. The lattice thermalization much slower than the formation of quasi-equilibrium point for the magnetic moment direction evinces the engagement of a nonthermal origin for the coherent magnon.

It is noteworthy to mention that the magnetic Bragg intensity change observed for laser fluences below  $2 \text{ mJ cm}^{-2}$  is not significantly influenced by the peak shift and broadening. The maximum values of peak shift and broadening for  $2 \text{ mJ cm}^{-2}$ , determined through linear interpolation from the values obtained at  $8.3 \text{ mJ cm}^{-2}$  (Figure 4b), are  $\Delta(2\theta) \approx -0.07^\circ$  and  $\Delta\text{peak-width}$  change of  $\approx 0.6^\circ$ . These changes are insignificant when compared to the relatively broad FM (0 0 3) Bragg peak, which has a FWHM (full-width-at-half-maximum) of  $\approx 3^\circ$  for the negative time delay in the resonant X-ray diffraction condition at  $E_i = 711 \text{ eV}$  (Figure 4b). The mosaicity of the magnetic Bragg peak is  $0.2^\circ$  in the FWHM (see Figure S10, Supporting Information), which is still considerably broader than the estimated  $\Delta\theta \approx -0.035^\circ$ .

## 2.4. Photoinduced Effective Magnetic Field

We note that the 4D trajectory of the magnon is able to elucidate the cause of the large change of magnetization. We first rule out ICME (inverse Cotton–Mouton effect)<sup>[17,18,22]</sup> and IMR (inverse magneto-refraction)<sup>[7,8]</sup> for photoinduced effective magnetic field available by the linearly polarized pump laser. These effects are present only when the laser pulse resides in the sample and thereby leads a magnetic moment to precess around its

original position after the pulse is gone, which are disagreed by the formation of the new quasi-equilibrium position (Figure 3e).

Instead, we find that nonthermal DECM (displacive excitation of coherent magnon) effect is consistent with our observation.<sup>[16]</sup> This effect produces a long-lived, photoinduced magnetic field ( $H_{\text{photo}}$ ), which is described as:<sup>[1,16]</sup>

$$H_{\text{photo}} = \chi_{ijkl} E_i E_k M_l \quad (2)$$

where  $\chi_{ijkl}$  is components of a fourth-rank magnetoelectric tensor related to the magnetic symmetry,  $E_{j(k)}$  is electric-field components inside the BSZFAO launched by the pump laser (long living even after the pump duration, to be discussed later), and  $M_l$  is components of the magnetic moment at the initial equilibrium position. The transverse conical order in the BSZFAO has the magnetic symmetry with nonzero  $\chi_{ijkl}$  components that allow the net of  $H_{\text{photo}}$  to be axial to the magnetization ( $M_x$ ) with not only p-polarization but also s-polarization of the pump laser. The  $H_{\text{photo}}$  direction turns out to be opposite to  $M_x$ . We confirmed the qualitatively similar intensity oscillations in the AFM (0 0 1.5) Bragg reflection for both polarizations (Figure S11, Supporting Information), while the quantitative difference is attributed to the polarization dependence of either the laser absorption or the magnetoelectric tensor component,  $\chi_{ijkl}$ .

The magnitude of  $H_{\text{photo}}$  can be quantified based on the quasi-equilibrium position determined in the 4D precession trajectory. We evaluate  $\Delta M_x$  at this quasi-equilibrium position, and then deduce the corresponding  $H_{\text{photo}}$  through the  $M_x$  vs  $H_{\text{ext}}$

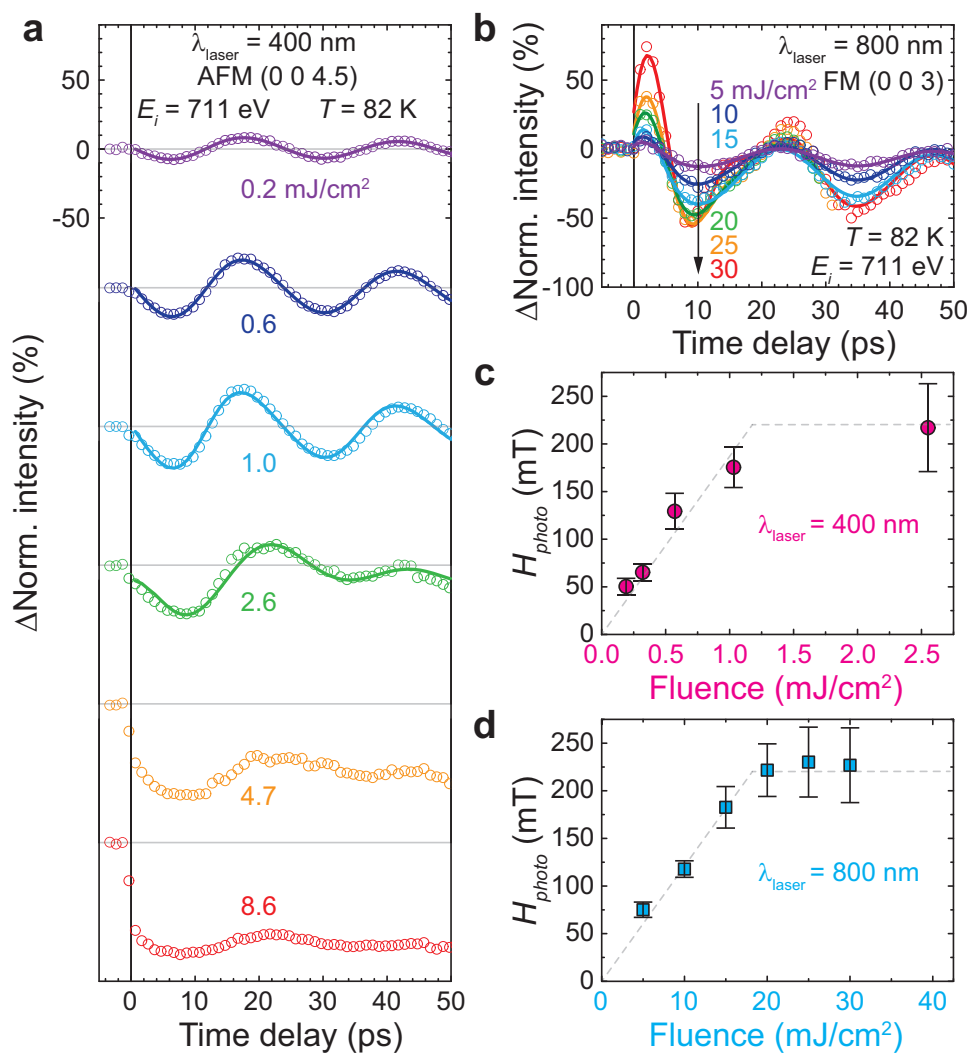


**Figure 5.** Effective magnetic field changes due to the laser excitation. a) AFM (0 0 4.5) intensities (circles) and their fit (solid curve) at  $H_{\text{ext}} (= 200 \text{ mT}) \parallel +x$  and  $T = 82 \text{ K}$  using incident X-ray energy,  $E_i = 711 \text{ eV}$  for the laser pump with  $\lambda_{\text{laser}} = 400 \text{ nm}$  (above the bandgap). The data for each fluence are vertically shifted for clarity. The gray lines denote initial intensities. b) FM (0 0 3) intensities (circles) and their fit (solid curve) under the same experimental condition except the laser pump with  $\lambda_{\text{laser}} = 800 \text{ nm}$  (below the bandgap). c,d) The laser fluence dependence of  $H_{\text{photo}}$  estimated from the coherent magnon trajectory for  $\lambda_{\text{laser}} = 400 \text{ nm}$  (pink circles) (c) and  $800 \text{ nm}$  (cyan squares) (d). The dashed lines are guides to the eye. The error bars are determined by the range of fitting parameters that give 10% increase of the least-squares values from the best fitting result.

relation, assuming  $\Delta H_{\text{ext}} = -|H_{\text{photo}}|$ . **Figure 5c** shows  $H_{\text{photo}}$  as a function of laser fluence that follows a linear slope below  $1.0 \text{ mJ cm}^{-2}$  in good agreement with Equation 2 (e.g.,  $E^2 \propto \text{fluence}$ ) and then becomes saturated. At higher fluences, it is hard to determine  $H_{\text{photo}}$  because the intensity oscillation profile is distorted by other effects such as ultrafast demagnetization<sup>[45]</sup> or magnetic-order melting<sup>[28,29,46]</sup> within 1 ps, the redshifting of the magnon frequency caused by a substantial increase of temperature after 10 ps, and the irregular oscillation amplitude possibly due to enhanced magnon–magnon or magnon–phonon scatterings (Figure 5a). To confirm the trend of  $H_{\text{photo}}$  upon the laser fluence, we switch  $\lambda_{\text{laser}}$  from 400 nm (the photon energy above the bandgap) to 800 nm (below the bandgap) (Figure 5b). The behaviors of  $H_{\text{photo}}$  for both laser wavelengths qualitatively agree well with each other, except that  $\lambda_{\text{laser}} = 800 \text{ nm}$  requires a 15 times

higher fluence compared to  $\lambda_{\text{laser}} = 400 \text{ nm}$  to achieve the same level of  $H_{\text{photo}}$  (Figure 5d). [The initial increase of FM (0 0 3) intensities before 2 ps in Figure 5b is attributed to a different origin.]

We remark that the overall fluence dependence in Figure 5c,d is in stark contrast with that for the coherent magnon driven by photoinduced strain on the lattice.<sup>[45,47–49]</sup> The photoexcitation above and below the bandgap are able to produce the strain through one-photon and two-photon absorption processes, respectively. In turn, the magnitudes of strain and its resultant coherent magnon follow linear and quadratic dependence on the laser fluence for the former and the latter, respectively, which contradicts our result in Figure 5c,d. Besides, the oscillation profiles measured with  $E_i = 702$  and  $711 \text{ eV}$  penetrating differently deep into the sample, match each other by adjusting their scale of amplitude to the penetration mismatch. If the strain propagating

from the sample surface were involved in generating the coherent magnon, both profiles would be qualitatively different. For instance, the signal measured with the X-ray probe at  $E_i = 702$  eV penetrating deeper than the laser pump with  $\lambda_{\text{laser}} = 400$  nm would be influenced by the strain after about tens of picosecond (see Figure S3, Supporting Information).

## 2.5. Possible Microscopic Mechanism

The photoexcitation above the bandgap yields significant photon absorption that generally obscures the influence on the photomagnetic effect due to other myriad photoinduced phenomena, e.g., demagnetization, magnetoelastic effect, and so on.<sup>[27–29,32]</sup> We remark that the 4D trajectory of the precessing magnetic moment enables clear access to the photomagnetic effect against the complication of the above-bandgap photoexcitation. This unique merit allows us to find a remarkably large amplification of the photomagnetic coupling. The coupling strength determined by the linear slope of  $H_{\text{photo}}$  vs fluence presents  $187 \pm 13$  mT cm<sup>2</sup> mJ<sup>−1</sup> for the above-bandgap photoexcitation ( $\lambda_{\text{laser}} = 400$  nm), which is much larger than  $12.3 \pm 0.5$  mT cm<sup>2</sup> mJ<sup>−1</sup> for the below-bandgap photoexcitation ( $\lambda_{\text{laser}} = 800$  nm). This amplified photomagnetic coupling is at least an order of magnitude higher than those in other AFM dielectrics, which have been characterized only for the below-bandgap photoexcitation<sup>[4,7,9,16]</sup> due to the difficulty aforementioned for the time-resolved magneto-optical spectroscopy. Note that the realized  $H_{\text{photo}} = 187$  mT with the fluence of  $1.0$  mJ cm<sup>−2</sup> for  $\lambda_{\text{laser}} = 400$  nm, is as strong as the field strength of rare-earth permanent magnets widely used in practice. This level of  $H_{\text{photo}}$  may flip the magnetization with a single-laser shot in a magnet, if the coercive magnetic field is small.

The enhanced photomagnetic coupling in the BSZFAO is understood based on the microscopic origin for DECM effect.<sup>[1,16]</sup> This effect relies on photoinduced electron redistribution among multivalent magnetic ions, which lasts long even after the photoirradiation. For example, iron garnets are known to have the nonthermal valence exchange persisting longer than a few nanoseconds, resulting in a quasi-static photoinduced magnetic anisotropy (PMA) that essentially works as a photoinduced magnetic field.<sup>[16]</sup> This microscopic process is known for the below-bandgap photoexcitation, but in principle also available for the above-bandgap photoexcitation. We note that a similar valence exchange channel is allowed for the BSZFAO. Its oxygen vacancy induced during the single crystal growth yields the multivalent iron ions distributed on tetrahedral/octahedral sites.<sup>[50]</sup> This situation is analogous to that in the iron garnets. Therefore, the enhancement of photomagnetic coupling in the BSZFAO implies higher efficiency in the valence exchange process through the charge transfer transition above the bandgap than the d–d transition below the bandgap. This route to boost the photomagnetic effect will be also effective for a variety of AFM dielectrics.

## 3. Conclusion

The 4D visualization of the coherent magnon realizes a long-anticipated capability of XFELs for investigating ultrafast nonequilibrium magnetic phenomena. This allows us to unambiguously identify the photoinduced magnetic field for both

above- and below-bandgap photoexcitation in a Y-type hexaferrite. We find that a remarkable amplification of the photomagnetic effect is achieved by the photoexcitation above the bandgap, which accounts for a large modulation of the net magnetization through the photoexcited AFM magnon. The notion that this hexaferrite is a multiferroic with ferroelectricity and ferrimagnetism strongly coupled to each other, suggests application prospects not only for optospintronics but also for ultrafast optical control of magnetoelectric effects.<sup>[33–35]</sup> This work fully demonstrates the advantages of resonant and nonresonant X-ray diffraction experiments brought into the ultrafast time domain, and further extends one's capability of revealing nonthermal phenomena in quantum materials with complex coupling among the fundamental physical degrees of freedom.

## 4. Experimental Section

**Sample Preparation and Characterization:** Single crystals of Ba<sub>0.5</sub>Sr<sub>1.5</sub>Zn<sub>2</sub>(Fe<sub>1−x</sub>Al<sub>x</sub>)<sub>12</sub>O<sub>22</sub> ( $x = 0.08$ ) (BSZFAO) were grown from Na<sub>2</sub>O–Fe<sub>2</sub>O<sub>3</sub> flux in air. The chemicals were prepared with the molar ratio, BaCO<sub>3</sub>:SrCO<sub>3</sub>:ZnO:Fe<sub>2</sub>O<sub>3</sub>:Al<sub>2</sub>O<sub>3</sub>:Na<sub>2</sub>O = 19.69(1 −  $x'$ ):19.69 $x'$ :19.69:53.61(1 −  $x$ ):53.61 $x$ :7.01, heated up to 1420 °C, and underwent a series of thermal cycles. The  $x'$  (= 0.85) and the thermal cycles followed the conditions in ref. [51].

An epitaxial thin film of BaFe<sub>10.2</sub>Sc<sub>1.8</sub>O<sub>19</sub> (M-type hexaferrite) with thickness = 74 nm was grown on the Al<sub>2</sub>O<sub>3</sub> (00.1) substrate by pulsed laser deposition under the same growth conditions as in ref. [52] and annealed ex situ twice, 2 hours at 930 °C and 2 hours at 1000 °C under flowing O<sub>2</sub> atmosphere. The film thickness and crystal structure were confirmed by X-ray reflectometry and X-ray diffraction measurements (out-of-plane and  $\Phi$ -scans), respectively, using a Panalytical X'Pert MRD diffractometer (Philips) equipped with a four bounce Ge (2 2 0) monochromator and a Cu K $\alpha_1$  radiation source.

The magnetization vs magnetic field curve for the BSZFAO single crystal was measured by using a vibrating sample magnetometer incorporated with PPMS (Quantum Design).

**Time-Resolved Resonant Magnetic X-ray Diffraction Experiment:** The optical laser pump and X-ray probe experiment was carried out using the RSXS (Resonant Soft X-ray Scattering) instrument in the soft X-ray beamline of PAL-XFEL.<sup>[53]</sup> The BSZFAO single crystal was mounted on a six-axis open-flow cryostat manipulator inside an ultrahigh vacuum chamber. The sample was cooled down to  $T = 82$  K with an external magnetic field ( $H_{\text{ext}} = 200$  mT) applied along the  $x$ -axis in the  $ab$ -plane. A pair of Nd–Fe–B magnets were attached to the sample holder and rotated together with the sample when the azimuthal angle was changed.

The optical laser pump was tuned to the wavelength = 400 or 800 nm, the pulse duration  $\approx 100$  fs, and the repetition rate = 30 Hz. The laser was horizontally polarized (i.e., p-polarization) and was incident on the sample in parallel to the X-ray probe. The time delay between the optical laser pump and the X-ray probe was controlled by a motorized linear stage.

The X-ray pulses were generated to have a pulse duration of  $\approx 80$  fs and the repetition rate = 60 Hz. The horizontally polarized X-ray and 2 $\theta$  rotation of the detector established the horizontal scattering geometry resulting in incident  $\pi$ -polarization. The scattered X-ray pulses were detected by an avalanche photodiode whose signals were recorded by a high-speed digitizer. The incident X-ray photon energy was calibrated from the X-ray absorption spectrum (XAS) of 100 nm-thick Fe foil measured via the transmission mode across the Fe L<sub>3</sub> edge. The repetition rate of the X-ray twice that of the optical laser pump allowed to compare the sample signals with/without the pumping for each time delay. This alternating probe removed errors from the mid- and long-term variations of the X-ray intensity.

**Penetration Depth of the X-rays:** The X-ray penetration depth at  $E_i = 702$  eV, just below the Fe L<sub>3</sub> edge  $\approx 710$  eV, was calculated to be 363 nm (density = 5.14 g cm<sup>−3</sup>, incident X-ray angle = 90°) from the database of



the Center for X-ray Optics.<sup>[54]</sup> It is well known that these calculations are accurate for X-ray energies away from the absorption edge. To estimate the penetration depth at the edge at 711 eV more precisely, the intensity ratio  $\approx 9.26$  of the XAS spectrum at the pre-edge and the absorption edge were taken into account.<sup>[44]</sup> The penetration depth was deduced to be 39 nm by dividing the depth at  $E_i = 702$  eV by the XAS intensity ratio. In the actual experimental geometry with an incident angle ( $\theta$ ), the penetration depths calculated for normal incidence needed to be multiplied by the factor of  $\sin(\theta)$ . In the geometries of the (0 0 3) Bragg reflection with an angle of  $\theta \approx 29^\circ$  and the (0 0 4.5) Bragg reflection with an angle of  $\theta \approx 66^\circ$ , the penetration depths from the sample surface were estimated to be 19 and 36 nm, respectively at  $E_i = 711$  eV.

**Penetration Depth of the Optical Laser.** Optical transmittance measurement by the UV–vis–NIR spectroscopy identified the absorption coefficient and penetration depth of the sample in the wavelength range. The BSZFAO single crystal was attempted to measure, but it was too thick ( $\approx 200$   $\mu\text{m}$ ) to obtain any relevant signal, absorbing almost all the incident photons. Alternatively, an epitaxial thin film of  $\text{BaFe}_{10.2}\text{Sc}_{1.8}\text{O}_{19}$  (M-type hexaferrite) with thickness = 74 nm was measured to estimate the penetration depth.<sup>[52]</sup> This M-type hexaferrite is known to have material properties in common with the BSZFAO, such as the transverse conical magnetic structure and magnetoelectricity.<sup>[52]</sup> Figure S1 (Supporting Information) shows a substantial rise of the absorption coefficient above 2.85 eV (blue), indicating the direct electronic bandgap. The penetration depth reduced abruptly around this wavelength and was counted to be 39 nm at  $\lambda_{\text{laser}} = 400$  nm. Later, the absorption coefficient (red, Figure S1, Supporting Information) of the BSZFAO was obtained by the optical ellipsometry measurement using M-2000 (J. A. Woollam Co.). Figure S1 (Supporting Information) shows that the BSZFAO has a direct bandgap = 2.75 eV and the penetration depth = 30 nm for  $\lambda_{\text{laser}} = 400$  nm (3.10 eV, above the bandgap) and 263 nm for  $\lambda_{\text{laser}} = 800$  nm (1.55 eV, below the bandgap). In the experimental setup where the optical laser pump and X-ray probe were incident collinearly on the sample, the penetration depths from the sample surface were calculated with the penetration depths for normal incidence multiplied by the factor of  $\sin(\theta)$ : in the geometries of the (0 0 3) Bragg reflection ( $\theta \approx 29^\circ$ ) and (0 0 4.5) Bragg reflection ( $\theta \approx 66^\circ$ ), 15 and 27 nm, respectively for  $\lambda_{\text{laser}} = 400$  nm, and 131 and 237 nm, respectively for  $\lambda_{\text{laser}} = 800$  nm.

**Fitting of the Transient Magnetic Bragg Peak Intensities.** The magnetic Bragg peak intensities in Figure 2a are fit with a damped oscillation and an exponential decay:

$$I = A_1 \exp(-t/\tau_1) \sin\left[\frac{2\pi(t-t_1)}{\Omega}\right] - A_2 \exp(-t/\tau_2) + A_3 \quad (3)$$

where  $t$  is the time delay,  $t_1$  is a phase shift,  $\Omega$  is the oscillation period, and  $\tau_1$  is a damping constant for the oscillation and  $\tau_2$  the exponential decay constant;  $A_1$ ,  $A_2$  are amplitudes of the oscillation and the decay, respectively, and  $A_3$  represents a constant background. The values extracted from the fit to the data in Figure 2a are summarized in Table S1 (Supporting Information).

**Magnetic Hamiltonian Model Calculation.** The  $M_x$  vs  $H_{\text{ext}}$  relation was deduced from the magnetic Hamiltonian (Equation 1) minimized with respect to the  $\mu_L$  and  $\mu_S$  directions.<sup>[41]</sup> The  $\mu_{L1}$ ,  $\mu_{L2}$ ,  $\mu_{S1}$ , and  $\mu_{S2}$  vectors constructing the transverse conical magnetic structure (the right panel of Figure 1a) are represented as:

$$\begin{pmatrix} \mu_{L1}^x \\ \mu_{L1}^y \\ \mu_{L1}^z \end{pmatrix} = \begin{pmatrix} \mu_L \cos\phi \\ -\mu_L \sin\phi \\ 0 \end{pmatrix}, \quad \begin{pmatrix} \mu_{L2}^x \\ \mu_{L2}^y \\ \mu_{L2}^z \end{pmatrix} = \begin{pmatrix} \mu_L \cos\phi \\ \mu_L \sin\phi \\ 0 \end{pmatrix} \quad (4)$$

$$\begin{pmatrix} \mu_{S1}^x \\ \mu_{S1}^y \\ \mu_{S1}^z \end{pmatrix} = \begin{pmatrix} -\mu_S \sin\theta \\ 0 \\ -\mu_S \cos\theta \end{pmatrix}, \quad \text{and} \quad \begin{pmatrix} \mu_{S2}^x \\ \mu_{S2}^y \\ \mu_{S2}^z \end{pmatrix} = \begin{pmatrix} -\mu_S \sin\theta \\ 0 \\ \mu_S \cos\theta \end{pmatrix} \quad (5)$$

where  $\phi$  and  $\theta$  are angles between  $\mu_L$  and the x-axis, and  $\mu_S$  and the z-axis, respectively. The magnetic Hamiltonian (Equation (1)) can be reformulated as:

$$\begin{aligned} \mathcal{H} = & -4J_{LS}\mu_L\mu_S \cos\phi \sin\theta + 2J_{LL}(\mu_L)^2 (\cos^2\phi - \sin^2\phi) \\ & + 2J_{SS}(\mu_S)^2 (\sin^2\theta - \cos^2\theta) + 2D_S(\mu_S)^2 \cos^2\theta \\ & - 2(H_{\text{int}} + H_{\text{ext}}) (\mu_L \cos\phi - \mu_S \sin\theta) \end{aligned} \quad (6)$$

Minimizing the Hamiltonian with respect to the  $\mu_L$  and  $\mu_S$  directions or  $\phi$  and  $\theta$  angles,

$$\left. \frac{\partial \mathcal{H}}{\partial \phi} \right|_{\theta} = \{4J_{LS}\mu_S \sin\theta - 8J_{LL}\mu_L \cos\phi + 2(H_{\text{int}} + H_{\text{ext}})\} (\mu_L \sin\phi) = 0 \quad (7)$$

$$\left. \frac{\partial \mathcal{H}}{\partial \theta} \right|_{\phi} = \{-4J_{LS}\mu_L \cos\phi + 8J_{SS}\mu_S \sin\theta - 4D_S\mu_S \sin\theta + 2(H_{\text{int}} + H_{\text{ext}})\} (\mu_S \cos\theta) = 0 \quad (8)$$

When the external magnetic field,  $H_{\text{ext}}$ , is increased to 1.59 T, it is known that  $\phi$  gradually decreases to zero, while  $\theta$  remains finite.<sup>[37]</sup> In the region of  $H_{\text{ext}} < 1.59$  T, the aforementioned minimization conditions lead to

$$\begin{aligned} M_x (\mu_B/\text{f.u.}) = & \mu_{L1}^x + \mu_{S1}^x = \mu_L \cos\phi - \mu_S \sin\theta \\ = & \frac{\{2J_{LS} - 2J_{LL} - (2J_{SS} - D_S)\}}{2\{J_{LS}^2 - 2J_{LL}(2J_{SS} - D_S)\}} (H_{\text{int}} + H_{\text{ext}}) \end{aligned} \quad (9)$$

while in the region of  $H_{\text{ext}} \geq 1.59$  T, as  $\phi$  is fixed to zero,

$$\begin{aligned} M_x (\mu_B/\text{f.u.}) = & \mu_{L1}^x + \mu_{S1}^x = \mu_L - \mu_S \sin\theta = \frac{2\{(2J_{SS} - D_S) - J_{LS}\} \mu_L}{2(2J_{SS} - D_S)} \\ & + \frac{1}{2(2J_{SS} - D_S)} (H_{\text{int}} + H_{\text{ext}}) \end{aligned} \quad (10)$$

The  $M_x$  vs  $H_{\text{ext}}$  relation was represented with these two linear lines with a change in slope at  $H_{\text{ext}} = 1.59$  T.

The net moments of the L and S blocks were set as  $|\mu_L| = 17.5 \mu_B$  and  $|\mu_S| = 4 \mu_B$  with the notion that interlayer spins of  $\text{Fe}^{3+}$  ions within each block are in antiparallel and unequal numbers of  $\text{Fe}^{3+}$  sites at different layers result in the uncompensated moments. It was found that the  $M_x$  vs  $H_{\text{ext}}$  relation with  $J_{LS}|\mu_L||\mu_S| = 85.3 \mu_B \text{ T}$ ,  $J_{LL}|\mu_L|^2 = 54.8 \mu_B \text{ T}$ ,  $J_{SS}|\mu_S|^2 = (40 + 0.8 D_S) \mu_B \text{ T}$ , and  $H_{\text{int}} = 1.21 \text{ T}$  is in good agreement with the experimental data (Figure 3a). Incorporating the Dzyaloshinskii–Moriya interaction into the magnetic Hamiltonian and adjusting the  $M_x$  vs  $H_{\text{ext}}$  relation might improve the correspondence between the calculated results and experimental data.<sup>[41]</sup> However, it was inferred that the interaction still had a minor impact as indicated by the small deviation observed in Figure 3a.

The parameters and relation obtained above were employed to determine the magnetic anisotropy constants,  $D_L$  and  $D_S$ . To this end, the Landau–Lifshitz–Gilbert equations (without damping terms for simplicity) were used that are written:

$$\frac{d}{dt} (\vec{\mu}_L) = -\gamma (\vec{\mu}_L \times \vec{H}_L) \quad \text{and} \quad \frac{d}{dt} (\vec{\mu}_S) = -\gamma (\vec{\mu}_S \times \vec{H}_S) \quad (11)$$

where  $\gamma$  is the gyromagnetic ratio and  $\vec{H}_{L(S)} = -\nabla_{\mu_{L(S)}} \mathcal{H}$  is the effective magnetic field on the L(S) block. The solutions taking into account AFM precessions of  $\mu_{L1}$  and  $\mu_{L2}$ , and  $\mu_{S1}$  and  $\mu_{S2}$  reveal two  $k = 0$  normal AFM magnon modes (Note S1, Supporting Information).<sup>[41]</sup> The lower energy AFM magnon (low-lying mode) was attributed to the coherent magnon with the frequency of  $41.7 \pm 0.9 \text{ GHz}$ .<sup>[40]</sup> The higher energy AFM

magnon (high-lying mode) was presumed in the frequency range 0.5–1.5 THz where a number of Y-type hexaferrites exhibited another AFM magnon mode.<sup>[42,43]</sup> By setting the frequency of this higher energy mode to 0.8 THz, it was found that  $D_L|\mu_L|^2 = 11.6 \mu_B$  T and  $D_S|\mu_S|^2 = -54.4 \mu_B$  T.

With all the parameters determined in the magnetic Hamiltonian, relative magnitudes of the AFM magnon modes were calculated. Figure S2 (Supporting Information) shows the trajectories of the lower- and higher-frequency modes. The former mode had dominant  $\mu_L$  precession of which trajectory was nearly isotropic, while  $\mu_S$  precession was insignificant and highly anisotropic along the x-axis. On the other hand, the latter mode exhibited comparable magnitudes of the  $\mu_L$  and  $\mu_S$  precessions that were largely elongated along the z-axis and nearly circular, respectively.

## Supporting Information

Supporting Information is available from the Wiley Online Library or from the author.

## Acknowledgements

This work was supported by the National Research Foundation of Korea (2019R1F1A1060295, 2019R1C1C1010034, 2019K1A3A7A09033399, 2019R1A2C2090648, 2020R1C1C1010477, 2022M3H4A1A04074153). The time-resolved resonant magnetic X-ray diffraction experiment was performed using the RSXS instrument at PAL-XFEL (Proposal No. 2021-2nd-SSS-022) funded by the Ministry of Science and ICT of Korea. H.U. and U.S. were supported by the National Centers of Competence in Research in Molecular Ultrafast Science and Technology (NCCR MUST-No. 51NF40-183615) from the Swiss National Science Foundation and from the European Union's Horizon 2020 research and innovation programme under the Marie Skłodowska–Curie Grant Agreement No. 801459-FP-RESOMUS. P.B. was supported by the EPSRC under EP/H000925 and by the European Union by the SOPRANO Marie-Curie ITN (Grant No. PITN-GA-2008-214040). M.J.R. thanks the Royal Society for the award of a Research Professor position.

## Conflict of Interest

The authors declare no conflict of interest.

## Data Availability Statement

The data that support the findings of this study are available from the corresponding author upon reasonable request.

## Keywords

multiferroic materials, photomagnetic effect, time-resolved resonant magnetic X-ray diffraction, X-ray free electron laser

Received: April 2, 2023  
Revised: June 27, 2023  
Published online: July 24, 2023

- [1] A. Kirilyuk, A. V. Kimel, T. Rasing, *Nature* **2010**, *82*, 2731.
- [2] B. A. Ivanov, *Low Temp. Phys.* **2014**, *40*, 91.
- [3] P. Němec, M. Fiebig, T. Kampfrath, A. V. Kimel, *Nat. Phys.* **2018**, *14*, 229.

- [4] A. V. Kimel, A. Kirilyuk, P. A. Usachev, R. V. Pisarev, A. M. Balbashov, T. Rasing, *Nature* **2005**, *435*, 655.
- [5] P. Němec, E. Rozkotová, N. Tesařová, F. Trojánek, E. De Ranieri, K. Olejník, J. Zemen, V. Novák, M. Cukr, P. Malý, T. Jungwirth, *Nat. Phys.* **2012**, *8*, 411.
- [6] N. Tesařová, P. Němec, E. Rozkotová, J. Zemen, T. Janda, D. Butkovičová, F. Trojánek, K. Olejník, V. Novák, P. Malý, T. Jungwirth, *Nat. Photonics* **2013**, *7*, 492.
- [7] R. V. Mikhaylovskiy, E. Hendry, A. Secchi, J. H. Mentink, M. Eckstein, A. Wu, R. V. Pisarev, V. V. Kruglyak, M. I. Katsnelson, Th. Rasing, A. V. Kimel, *Nat. Commun.* **2015**, *6*, 8190.
- [8] R. V. Mikhaylovskiy, T. J. Huisman, V. A. Gavrichkov, S. I. Polukeev, S. G. Ovchinnikov, D. Afanasiev, R. V. Pisarev, Th. Rasing, A. V. Kimel, *Phys. Rev. Lett.* **2020**, *125*, 157201.
- [9] T. F. Nova, A. Cartella, A. Cantaluppi, M. Först, D. Bossini, R. V. Mikhaylovskiy, A. V. Kimel, R. Merlin, A. Cavalleri, *Nat. Phys.* **2017**, *13*, 132.
- [10] A. S. Disa, M. Fechner, T. F. Nova, B. Liu, M. Först, D. Prabhakaran, P. G. Radaelli, A. Cavalleri, *Nat. Phys.* **2020**, *16*, 937.
- [11] D. Afanasiev, J. R. Hortensius, B. A. Ivanov, A. Sasani, E. Bousquet, Y. M. Blanter, R. V. Mikhaylovskiy, A. V. Kimel, A. D. Caviglia, *Nat. Mater.* **2021**, *20*, 607.
- [12] A. Stupakiewicz, C. S. Davies, K. Szerenos, D. Afanasiev, K. S. Rabinovich, A. V. Boris, A. Caviglia, A. V. Kimel, A. Kirilyuk, *Nat. Phys.* **2021**, *17*, 489.
- [13] A. V. Kimel, A. Kirilyuk, A. Tsvetkov, R. V. Pisarev, Th. Rasing, *Nature* **2004**, *429*, 850.
- [14] A. de la Torre, D. M. Kennes, M. Claassen, S. Gerber, J. W. McIver, M. A. Sentef, *Rev. Mod. Phys.* **2021**, *93*, 041002.
- [15] T. Ogasawara, K. Ohgushi, Y. Tomioka, K. S. Takahashi, H. Okamoto, M. Kawasaki, Y. Tokura, *Phys. Rev. Lett.* **2005**, *94*, 087202.
- [16] F. Hansteen, A. Kimel, A. Kirilyuk, Th. Rasing, *Phys. Rev. Lett.* **2005**, *95*, 047402.
- [17] A. M. Kalashnikova, A. V. Kimel, R. V. Pisarev, V. N. Gridnev, A. Kirilyuk, Th. Rasing, *Phys. Rev. Lett.* **2007**, *99*, 167205.
- [18] R. Iida, T. Satoh, T. Shimura, K. Kuroda, B. A. Ivanov, Y. Tokunaga, Y. Tokura, *Phys. Rev. B* **2011**, *84*, 064402.
- [19] N. Kanda, T. Higuchi, H. Shimizu, K. Konishi, K. Yoshioka, M. Kuwata-Gonokami, *Nat. Commun.* **2011**, *2*, 362.
- [20] T. Satoh, R. Iida, T. Higuchi, M. Fiebig, T. Shimura, *Nat. Photonics* **2015**, *9*, 25.
- [21] V. Saidl, P. Němec, P. Wadley, V. Hills, R. P. Campion, V. Novák, K. W. Edmonds, F. Maccherazzi, S. S. Dhesi, B. L. Gallagher, F. Trojánek, J. Kuneš, J. Železný, P. Malý, T. Jungwirth, *Nat. Photonics* **2017**, *11*, 91.
- [22] L. Q. Shen, L. F. Zhou, J. Y. Shi, M. Tang, Z. Zheng, D. Wu, S. M. Zhou, L. Y. Chen, H. B. Zhao, *Phys. Rev. B* **2018**, *97*, 224430.
- [23] C. Tzschaschel, T. Satoh, M. Fiebig, *Nat. Commun.* **2019**, *10*, 3995.
- [24] N. P. Duong, T. Satoh, M. Fiebig, *Phys. Rev. Lett.* **2004**, *93*, 117402.
- [25] J. Wang, I. Cotoros, K. M. Dani, X. Liu, J. K. Furdyna, D. S. Chemla, *Phys. Rev. Lett.* **2007**, *98*, 217401.
- [26] Y. Hashimoto, S. Kobayashi, H. Muneoka, *Phys. Rev. Lett.* **2008**, *100*, 067202.
- [27] S. L. Johnson, R. A. de Souza, U. Staub, P. Beaud, E. Möhr-Vorobeve, G. Ingold, A. Caviezel, V. Scagnoli, W. F. Schlott, J. J. Turner, O. Krupin, W.-S. Lee, Y.-D. Chuang, L. Patthey, R. G. Moore, D. Lu, M. Yi, P. S. Kirchmann, M. Trigo, P. Denes, D. Doering, Z. Hussain, Z.-X. Shen, D. Prabhakaran, A. T. Boothroyd, *Phys. Rev. Lett.* **2012**, *108*, 037203.
- [28] M. P. M. Dean, Y. Cao, X. Liu, S. Wall, D. Zhu, R. Mankowsky, V. Thampy, X. M. Chen, J. G. Vale, D. Casa, Jung-Ho Kim, A. H. Said, P. Juhas, R. Alonso-Mori, J. M. Glownia, A. Robert, J. Robinson, M. Sikorski, S. Song, M. Kozina, H. Lemke, L. Patthey, S. Owada, T. Katayama, M. Yabashi, Yoshikazu Tanaka, T. Togashi, J. Liu, C. Rayan Serrao, B. J. Kim, et al., *Nat. Mater.* **2016**, *15*, 601.

- [29] D. G. Mazzone, D. Meyers, Y. Cao, J. G. Vale, C. D. Dashwood, Y. Shi, A. J. A. James, N. J. Robinson, J. Lin, V. Thampy, Y. Tanaka, A. S. Johnson, H. Miao, R. Wang, T. A. Assefa, J. Kim, D. Casa, R. Mankowsky, D. Zhu, R. Alonso-Mori, S. Song, H. Yavas, T. Katayama, M. Yabashi, Y. Kubota, S. Owada, J. Liu, J. Yang, R. M. Konik, I. K. Robinson, et al., *Proc. Natl. Acad. Sci. USA* **2021**, *118*, e2103696118.
- [30] B. W. J. McNeil, N. R. Thompson, *Nat. Photonics* **2010**, *4*, 814.
- [31] A. Stupakiewicz, K. Szerenos, D. Afanasiev, A. Kirilyuk, A. V. Kimel, *Nature* **2017**, *542*, 71.
- [32] M. Först, A. D. Caviglia, R. Scherwitzl, R. Mankowsky, P. Zubko, V. Khanna, H. Bromberger, S. B. Wilkins, Y.-D. Chuang, W. S. Lee, W. F. Schlotter, J. J. Turner, G. L. Dakovski, M. P. Minitti, J. Robinson, S. R. Clark, D. Jaksch, J.-M. Triscone, J. P. Hill, S. S. Dhesi, A. Cavalleri, *Nat. Mater.* **2015**, *14*, 883.
- [33] T. Kubacka, J. A. Johnson, M. C. Hoffmann, C. Vicario, S. de Jong, P. Beaud, S. Gröbel, S.-W. Huang, L. Huber, L. Patthey, Y.-D. Chuang, J. J. Turner, G. L. Dakovski, W.-S. Lee, M. P. Minitti, W. Schlotter, R. G. Moore, C. P. Hauri, S. M. Koohpayeh, V. Scagnoli, G. Ingold, S. L. Johnson, U. Staub, *Science* **2014**, *343*, 1333.
- [34] M. Matsubara, S. Manz, M. Mochizuki, T. Kubacka, A. Iyama, N. Aliouane, T. Kimura, S. L. Johnson, D. Meier, M. Fiebig, *Science* **2015**, *348*, 1112.
- [35] D. Bossini, K. Konishi, S. Toyoda, T. Arima, J. Yumoto, M. Kuwata-Gonokami, *Nat. Phys.* **2018**, *14*, 370.
- [36] S. H. Chun, Y. S. Chai, Y. S. Oh, D. Jaiswal-Nagar, S. Y. Haam, I. Kim, B. Lee, D. H. Nam, K.-T. Ko, J.-H. Park, J.-H. Chung, K. H. Kim, *Phys. Rev. Lett.* **2010**, *104*, 037204.
- [37] H. B. Lee, Y.-S. Song, J.-H. Chung, S. H. Chun, Y. S. Chai, K. H. Kim, M. Reehuis, K. Prokeš, S. Mat'áš, *Phys. Rev. B* **2011**, *83*, 144425.
- [38] T. Kimura, G. Lawes, A. P. Ramirez, *Phys. Rev. Lett.* **2005**, *94*, 137201.
- [39] K. Knížek, P. Novák, M. Küpferling, *Phys. Rev. B* **2006**, *73*, 153103.
- [40] D. Talbayev, S. A. Trugman, A. V. Balatsky, T. Kimura, A. J. Taylor, R. D. Averitt, *Phys. Rev. Lett.* **2008**, *101*, 097603.
- [41] S. H. Chun, K. W. Shin, H. J. Kim, S. Jung, J. Park, Y.-M. Bahk, H.-R. Park, J. Kyoung, D.-H. Choi, D.-S. Kim, G.-S. Park, J. F. Mitchell, K. H. Kim, *Phys. Rev. Lett.* **2018**, *120*, 027202.
- [42] N. Kida, D. Okuyama, S. Ishiwata, Y. Taguchi, R. Shimano, K. Iwasa, T. Arima, Y. Tokura, *Phys. Rev. B* **2009**, *80*, 220406.
- [43] J. Vít, F. Kadlec, C. Kadlec, F. Borodavka, Y. S. Chai, K. Zhai, Y. Sun, S. Kamba, *Phys. Rev. B* **2018**, *97*, 134406.
- [44] W.-S. Noh, K.-T. Ko, S. H. Chun, K. H. Kim, B.-G. Park, J.-Y. Kim, J.-H. Park, *Phys. Rev. Lett.* **2015**, *114*, 117603.
- [45] H. Ueda, H. Jang, S. H. Chun, H.-D. Kim, M. Kim, S.-Y. Park, S. Finizio, N. O. Hernandez, V. Ovuka, M. Savoini, T. Kimura, Y. Tanaka, A. Doll, U. Staub, *Phys. Rev. Res.* **2022**, *4*, 023007.
- [46] D. Afanasiev, A. Gatilova, D. J. Groenendijk, B. A. Ivanov, M. Gibert, S. Gariglio, J. Mentink, J. Li, N. Dasari, M. Eckstein, Th. Rasing, A. D. Caviglia, A. V. Kimel, *Phys. Rev. X* **2019**, *9*, 021020.
- [47] Y. Hashimoto, D. Bossini, T. H. Johansen, E. Saitoh, A. Kirilyuk, T. Rasing, *Phys. Rev. B* **2018**, *97*, 140404.
- [48] L. Soumah, D. Bossini, A. Anane, S. Bonetti, *Phys. Rev. Lett.* **2021**, *127*, 077203.
- [49] S. P. Zeuschner, J.-E. Pudell, A. von Reppert, M. Deb, E. Popova, N. Keller, M. Rössle, M. Herzog, M. Bargheer, *Phys. Rev. Res.* **2020**, *2*, 022013.
- [50] Y. S. Chai, S. H. Chun, S. Y. Haam, Y. S. Oh, I. Kim, K. H. Kim, *New J. Phys.* **2009**, *11*, 073030.
- [51] N. Momozawa, M. Mita, H. Takei, *J. Cryst. Growth* **1987**, *83*, 403.
- [52] P. Borisov, J. Alaria, T. Yang, S. R. C. McMitchell, M. J. Rosseinsky, *Appl. Phys. Lett.* **2013**, *102*, 032902.
- [53] H. Jang, H.-D. Kim, M. Kim, S. H. Park, S. Kwon, J. Y. Lee, S.-Y. Park, G. Park, S. Kim, H. Hyun, S. Hwang, C.-S. Lee, C.-Y. Lim, W. Gang, M. Kim, S. Heo, J. Kim, G. Jung, S. Kim, J. Park, J. Kim, H. Shin, J. Park, T.-Y. Koo, H.-J. Shin, H. Heo, C. Kim, C.-K. Min, J.-H. Han, H.-S. Kang, et al., *Rev. Sci. Instrum.* **2020**, *91*, 083904.
- [54] L. B. Henke, E. M. Gullikson, J. C. Davis, *At. Data Nucl. Data Tables* **1993**, *54*, 181.